Phase-Coherent Optical Frequency Up-Conversion with Millimeter-Size Zn(3-ptz)₂ Metal-Organic Framework Single Crystals

Diego Hidalgo-Rojas, Juan García-Garfido, Javier Enríquez, Ricardo Rojas-Aedo, Robert Alastair Wheatley, Rubén A. Fritz, Dinesh P. Singh, Felipe Herrera,* and Birger Seifert*

Metal-organic frameworks (MOFs) have emerged as candidate materials for nonlinear optics due to their enhanced optical and chemical stability in comparison with conventional organic crystals. However, producing large single crystals that support perfect phase matching conditions for frequency conversion is a long-standing challenge due to the highly metastable conditions in which MOF crystals tend to self-assemble in solution. By modulating the synthesis and growth conditions, this limitation is overcome to produce millimeter–sized Zn(3-ptz)₂ uniaxial MOF single crystals. Optimized MOF crystals with large birefringence in the visible $\Delta n \approx -0.3$ and high transparency allow for the observation of strong second-harmonic (SHG) and third-harmonic generation (THG) signals for the first time, using femtosecond near-infrared pump pulses. For conditions of type-I SHG phase-matching, the measured effective nonlinear coefficient of Zn(3-ptz)₂ is $d_{\mathrm{eff}} \approx 0.10\,\mathrm{pm\,V^{-1}}$, the largest measured nonlinearity for MOF materials to date. The experiments quantitatively agree with first-principles simulations based on the crystal lattice structure. The damage threshold is estimated on the order of 0.2 TW cm⁻² for raw single crystals, which can be further increased with additional crystal engineering steps. The demonstration of efficient frequency up-conversion of light with long-range phase coherence establishes MOF single crystals as promising materials for nonlinear optical devices.

1. Introduction

Metal-organic framework (MOF) crystals have attracted considerable interest in materials science because they can be tailored for specific applications.[1–3] The appropriate combination of organic molecular linkers and metal ion nodes, together with fine-tuned synthesis conditions, have enabled the development of MOFs exhibiting record-high porosity and surface area that results in outstanding performance for gas storage,[4,5] chemical sensing[6,7] and energy storage[8,9] applications. The intrinsic design flexibility of MOFs enables a convenient synergy between the structural stability of inorganic crystals and the strong electro-optical response of organic materials,[10–12] which makes MOF crystals attractive for nonlinear optics.

Several synthesis methods have been demonstrated for producing MOFs with second-order nonlinear optical response, by self-assembling organic ligands that have large hyper-polarizabilities with transition metal ions that enable the formation

D. Hidalgo-Rojas, R. A. Wheatley, B. Seifert
Facultad de Física
Pontificia Universidad Católica de Chile
Casilla 306, Santiago 22, 782-0436, Chile
E-mail: bseifert@fis.puc.cl

D. Hidalgo-Rojas, J. García-Garfido, J. Enríquez, R. A. Wheatley,
R. A. Fritz, D. P. Singh, F. Herrera, B. Seifert
Millennium Institute for Research in Optics
Concepción 407013, Chile
E-mail: felipe.herrera.u@usach.cl

J. García-Garfido, J. Enríquez, R. A. Fritz, D. P. Singh, F. Herrera
Department of Physics
Universidad de Santiago de Chile
Av. Victor Jara, Santiago 3493, Chile

R. Rojas-Aedo
Department of Physics and Materials Science
University of Luxembourg
Luxembourg 1511, Luxembourg

**ADVANCED
SCIENCE NEWS**

www.advancedsciencenews.com

**ADVANCED
OPTICAL
MATERIALS**

www.advopticalmat.de

of non-centrosymmetric coordination geometries.[10] Wide transparency windows for the resulting MOF crystals can be designed by selecting metal ions such as Zn^{2+} and Cd^{2+} with a complete d-shell that prohibits absorptive losses in the visible and suppresses undesired charge transfer processes that would otherwise make the crystals susceptible to oxidation under optical operation conditions.[13] Further enhancements of the second-order nonlinearities can be achieved by choosing organic ligands with electron-donor and electron-acceptor groups in their structure, which enables additional contributions to the nonlinear crystal polarization in response to external electromagnetic fields.[14]. Moreover, the electronic conjugation properties of organic ligands are also known to be the source of large third-order nonlinear optical susceptibilities for MOF crystals already in powder form.[15]

In the Cambridge Structural Database[16] there are a few thousand MOF crystals reported to date that would be suitable for second-harmonic generation (SHG) in modern laser and imaging devices[17–19] and integrated nonlinear photonics. For dozens of these nonlinear MOF crystals, SHG signals have been measured using polycrystalline samples with an ensemble of randomly-oriented crystal grains with an average size on the order of tens of micrometers.[10,12] In powder form, MOF samples only allow the observation of weak statistically-averaged nonlinear signals because morphological disorder along the optical path does not allow for long-range phase-matching in a wave mixing process. As a result of poor phase coherence, the SHG intensity of powder samples only scales linearly with the propagation length L[20,21] and the up-converted radiation typically spreads over a wide angular range,[10,21,22] which is undesirable for applications in coherent optics.[23–26] In contrast, a single crystal with the same propagation length gives a much brighter SHG output intensity scaling with L^2. Therefore, producing crystals with high optical transparency, large propagation lengths in the millimeter regime, large polished incidence areas, and high laser damage thresholds is an enabling step in the development of nonlinear optical devices based on crystalline MOF materials.

Growing MOF single crystals to millimeter dimensions is a significant challenge.[27–30] Unlike more commonly used nonlinear optical materials such as potassium dihydrogen phosphate KH_2PO_4 (KDP), of which the growth mechanism and kinetics are well known,[31] the general factors that control the self-assembly and crystallization mechanisms of MOF structures are largely unknown.[32–34] Recent progress in this direction was reported in Ref. [35], where a mechanistic study enabled the isolation of key reaction intermediates that control the self-assembly of Zn(3-ptz)$_2$ (MIRO-101), a non-centrosymmetric MOF crystal whose SHG activity was first observed in powder samples only.[36] A key step in the reaction mechanism is the formation of the metastable zwitterion 5-(pyridin-1-ium-3-yl)tetrazol-1-ide (3-Hptz) under acidic conditions. The presence of 3-Hptz in solution reduces the available concentration of the anionic species 5-(pyridin-3-yl)tetrazol-2-ide (3-ptz-), the organic ligand that feeds the growth of Zn(3-ptz)$_2$. Modulating the in situ formation of 3-ptz- therefore controls the nucleation and growth rates of Zn(3-ptz)$_2$, allowing for the formation of large MOF single crystal samples.

In this work, we optimize the synthesis and growth conditions of MIRO-101 single crystals to demonstrate the first millimeter-size MOF-based optical crystal device that simultaneously generates second-harmonic and third-harmonic (THG) radiation via up-conversion of near-infrared photons with coherent phase matching. The large crystal size allows for the determination of the ordinary and extraordinary refractive indices, demonstrating the large birefringence of this MOF material. The optical transparency of MIRO-101 and its effective nonlinear coefficient for type-I SHG are shown to be competitive with standard optical materials, highlighting the great potential of MOF materials for the development of nonlinear optical devices.

2. Results and Discussion

2.1. Metal-Organic Framework Single Crystals

Figure 1a shows the primitive cell of MIRO-101, with each zinc ion coordinating four pyridyl-tetrazolate (3-ptz) ligands forming a diamonoid coordination network without inversion symmetry. The 3-ptz ligands coordinate with zinc through the electron-aceptor tetrazole group, leaving a freely-rotating electron-donor pyridyl group. This rotation introduces a degree of crystallographic disorder at the growth temperature of 105 °C[30] that does not affect the optical transparency of the samples.[37] Figure 1b shows top and side views of one of the MIRO-101 crystal samples used to obtain the frequency conversion results discussed below. The top view highlights the birefringence. Figure 1c shows the optical transmittance of a representative cut and polished MIRO-101 crystal. From these measurements, the optical band gap $E_g = 3.71 \pm 0.01$ eV was obtained for millimeter-sized single crystals (see Figure S1, Supporting Information), consistent with previous measurements on polycrystalline samples.[37,38] Taking into account Fresnel reflections at the entrance and exit surfaces at normal incidence for both polarization components, the intrinsic optical transparency of the crystal in the spectral range 400–800 nm is estimated to exceed 95% in the region, where the SHG signal is expected (515 nm), which is comparable to commercial frequency-doubling crystals. Linear absorption at the band edge is only moderate in the region where the THG signal is expected (343 nm).

2.2. Birefringence Measurements

The birefringence of a millimeter-size MIRO-101 single crystal (see Figure 1b) was measured directly using a focused green laser beam ($\lambda = 517$ nm, $P = 0.9$ mW, cw) that undergoes ray-doubling upon transmission inside the MOF. The distance between the two transmitted beams at the end of the crystal was measured as a function of the angle of incidence. The two parallel output beams merge into a single beam when the beam direction is collinear with one of the three principal axes of the crystal. Linearly polarized light propagating along the optic axis (c-axis) does not change its polarization state. In this way, the optic axis could be uniquely assigned. To obtain the ordinary refractive index n_o, a simple and robust method for determining the refractive indices of plane plates was implemented.[39] Two different angular orientations of the crystal, which correspond to two different angles of incidence, generate a beam displacement between the ordinary beam emerging from the crystal and a reference beam that did
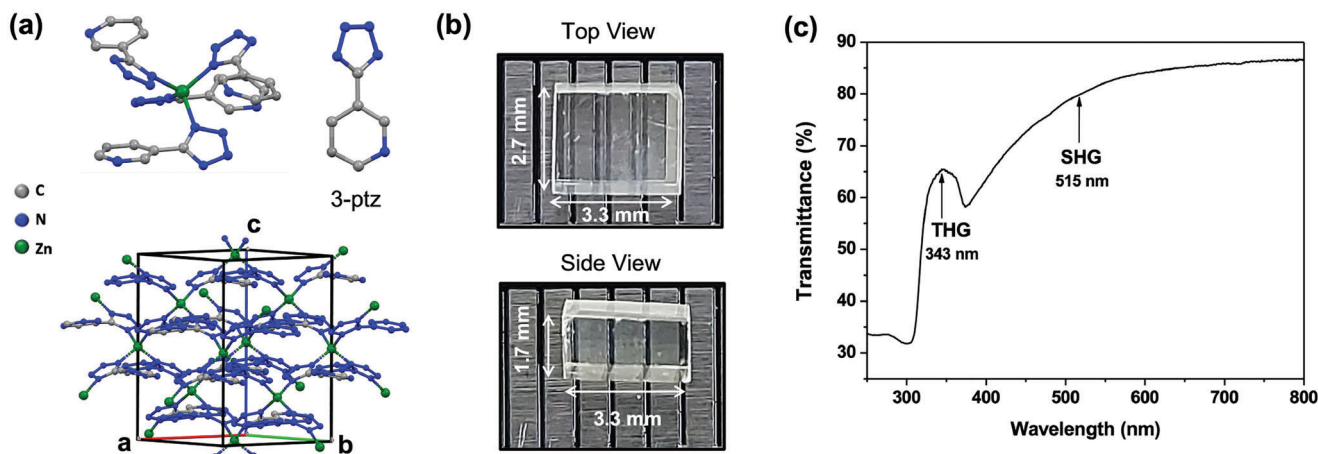
Figure 1. a) $Zn(3\text{-}ptz)_2$ (MIRO-101) MOF crystal structure (CSD:184958 [36]). The tetrahedral coordination geometry of the repeat unit and the chemical structure of the organic ligand (3-ptz) are also shown; b) Top and side views of one of the cut and polished MIRO-101 single crystal samples. The top view highlights the large crystal birefringence; c) Transmittance spectrum of the sample in panel (b). The high transparency at the second-harmonic ($\lambda_p/2$) and third-harmonic ($\lambda_p/3$) wavelengths are highlighted ($\lambda_p = 1030$ nm).

not pass through the crystal. By measuring the beam displacement, the ordinary refractive index $n_o = 1.8 \pm 0.1$ is obtained. The method was validated by reproducing the reported refractive index of a reference fused silica plate. Using the measured value of n_o, the extraordinary refractive index is obtained by estimating the birefringence angle at normal incidence, giving $n_e = 1.5 \pm 0.2$. These index measurements are in agreement with the theoretical Sellmeier curves obtained using periodic density-functional theory DFT ($n_o = 1.88$ and $n_e = 1.50$ at 517 nm[40], see also Section S2, Supporting Information), confirming that MIRO-101 is negative uniaxial. The birefringence of MIRO-101 $\Delta n \equiv n_e - n_o \approx -0.3$ is three times higher than the industry standard beta-barium borate β-BaB_2O_4 (BBO). Additional surface engineering of the crystals would allow for more precise methods for measuring the optical constants based on wave-front-shearing interferometry[41] or uniaxial Brewster angle reflectometry.[42,43]

2.3. Second-Harmonic Generation

SHG measurements were carried out by focusing near-infrared pump laser pulses on different MIRO-101 crystal samples, as illustrated in **Figure 2**a. For focused ultrafast pump lasers, the

transverse field profile needs to be considered to extract material parameters from the measured SHG power. When focusing a Gaussian beam into a nonlinear crystal, it is common to apply the Boyd-Kleinman focusing condition[44] $L/b = 2.84$, where L is the crystal length and b the confocal parameter. This ratio maximizes the SHG power, but inside the crystal the wavefront deviates significantly from a plane wave and the intensity of the pump beam is not constant along the propagation direction. Figure 2b describes the optical setup. The achromatic doublet lens, with a focal length of 50 mm, produces a Gaussian beam in air with beam divergence (full angle) $\Theta = 36 \pm 3$ mrad, beam waist $w_0 = 18.2 \pm 1.3$ μm, and Rayleigh range $z_R = 1.00 \pm 0.08$ mm. Under normal incidence, the Gaussian beam focused into a transparent crystal with planar surface does not change its beam waist, i.e., $w_{0, crystal} = w_{0, air}$[45] but the Rayleigh range increases inside the crystal to $z_{R, crystal} = n z_{R, air}$, where n is the refractive index of the crystal at the pump wavelength. The Rayleigh range of the pump beam inside the MOF crystal is thus $z_R = 1.83 \pm 0.15$ mm and $z_R = 1.66 \pm 0.14$ mm for a 1 mm thick reference BBO crystal (flatness $\lambda/8$ at 633 nm). In both cases, the values of L/b are much smaller than the Boyd-Kleinman focusing ratio ($L/b = 0.37 \pm 0.04$ for MOF and $L/b = 0.30 \pm 0.03$ for BBO), which
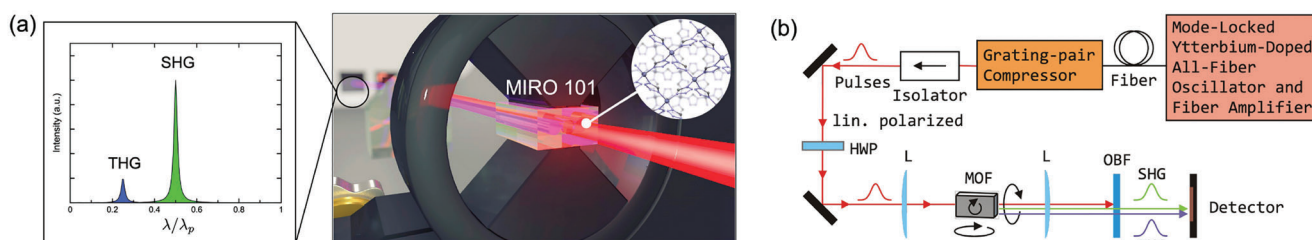

Figure 2. a) Illustration of the frequency up-conversion process. The pump laser beam of wavelength λ_p generates a second-harmonic signal at $\lambda_p/2$ and a third-harmonic signal at $\lambda_p/3$ by propagating through a MIRO-101 MOF crystal; b) Scheme of the optical setup: HWP, Achromatic half–wave plate for 690–1200 nm; L, Achromatic doublet lens with a focal length of 50 mm and antireflection coating for 400–1100 nm; MOF, $Zn(3-ptz)_2$ MOF crystal with three axes of rotation that run through the center of the MOF crystal; OBF, Optical bandpass filter that consists of two BG40 colored glass bandpass filters (335 nm – 610 nm) in a row.

**ADVANCED
SCIENCE NEWS**

www.advancedsciencenews.com

**ADVANCED
OPTICAL
MATERIALS**

www.advopticalmat.de

implies that the wavefront of the pump beam in both crystals is flat (plane waves) to a very good approximation. The beam radius is practically constant upon propagation to the beam waist w_0. Despite the slightly different refractive indices, the beam shape in both crystals is practically identical, because the Rayleigh range is larger than the crystal length. The longitudinal focus position has been optimized manually. Because of the same beam profiles in the crystals (only the crystal lengths are different) a comparison of the optical properties and the SHG outputs is straightforward.

The pump field comes from a fiber laser that generates ultrafast pulses with maximum pulse energy of 10 µJ and pulse duration of 340 fs. The pulse energy can be varied continuously. The pulse beam has a Gaussian profile with center wavelength λ_p = 1030 nm (see the pulse spectrum in Section S3, Supporting Information). The laser is seeded by a Yb:doped femtosecond fiber oscillator with a repetition rate of 29.2617 MHz. A pulse picker then reduces this frequency by a factor of 256 to 114.304 kHz. The laser is based on the chirped-pulse amplification (CPA) technique, and combines a Yb:doped fiber amplifier with a grating–pair pulse compressor, as shown in Figure 2b. The pulses from lasers based on the CPA technique frequently have complex temporal profiles because the pulse compression is imperfect. These temporal electric field characteristics can be accounted for by using a reference crystal. In this way, the temporal pulse profile does not need to be known. For femtosecond pulses, the chromatic dispersion of the crystal must also be taken into account, i.e., group velocity dispersion, temporal walk-off, and the spectral acceptance bandwidth, the latter is discussed below.

The center of the SHG output is expected at $\lambda_p/2$ = 515 nm under conditions of perfect phase matching (PPM). Although MIRO-101 crystals support both type-I and type-II phase matching conditions,[40] only degenerate type-I ooe (o+o → e) phase matching is measured here. The PPM condition for collinear type-I phase matching using ordinary-polarized pump pulses at λ_p = 1030 nm reduces to $n_o(\lambda_p) = n_e(\lambda_p/2, \theta)$, where θ is the polar angle between the propagation direction inside the crystal and the optic axis. From the calculated Sellmeier curves for $n_e(\lambda)$ and $n_o(\lambda)$ (see Section S2, Supporting Information), MIRO-101 crystals should satisfy PPM at $\theta = 21.7°$ when pumping at 1030 nm. Assuming low conversion efficiency (no pump depletion), the intensity of the pump beam I_p at the crystal entrance and the SHG intensity I_{SHG} at the crystal exit under conditions of PPM are given by [46]

$$I_{SHG} = \frac{2d_{eff}^2 \omega_p^2 L^2}{n_p^3 c_0^3 \varepsilon_0} I_p^2 \tag{1}$$

where L is the geometric path length that the beams traverse, approximated here by the crystal length, ω_p is the pump angular frequency, n_p pump refractive index and d_{eff} the effective nonlinear coefficient of the crystal. Equation 1 is strictly valid for plane waves with constant intensity in the beam cross-section, and should be corrected by a factor if Gaussian beams are used. However, this factor would be the same for the MOF and BBO reference, and therefore it is not important in the comparative analysis below. The effective nonlinear coefficient d_{eff} of MIRO-101 is determined relative to a commercial BBO crystal with known

d_{eff}. Since the beam parameters and detection setup are the same, the ratio of the nonlinear coefficients can be obtained from Equation 1 as

$$\frac{d_{eff,MOF}}{d_{eff,BBO}} = \left(\frac{n_{MOF}}{n_{BBO}}\right)^{3/2} \frac{L_{BBO}}{L_{MOF}} \frac{P_{BBO}}{P_{MOF}} \left(\frac{P_{SHG,MOF}}{P_{SHG,BBO}}\right)^{1/2} \tag{2}$$

where $n_{MOF} = 1.81$ and $n_{BBO} = 1.66$ are ordinary refractive indices at 1030 nm. The thickness of the polished MIRO-101 crystal used is $L_{MOF} = 1.35$ mm and $L_{BBO} = 1.00$ mm for BBO. Taking the ratio of the nonlinear coefficients makes the estimate independent of the pulse-dependent factors that convert from intensity I to power P.

Intense second harmonic green light at 515 ± 2 nm is generated by MIRO-101 single crystals upon illumination with 1030 nm pulses, as shown in **Figure 3**a for a polished crystal with few millimeter dimensions. For a raw as-synthesized crystal (Figure 3a, inset), the SHG signal is visible with the naked eye, as green light scatters through the crystal in all directions due to growth imperfections. After cutting and polishing the MOF samples, the SHG output beam leaves the crystal as a well-collimated, intense, and coherent light beam. No further amplification is needed for quantifying the nonlinear output, which significantly improves the SHG brightness over previous Kurtz-Perry measurements of Zn(3-ptz)$_2$ in powder form.[36] Figure 3a compares the measured SHG spectrum with an analytical curve based on theoretical Sellmeier curves that assume a monochromatic pump field (see Section S2, Supporting Information). Both theory and experiment show that the SHG spectral acceptance bandwidth of the crystal is $\delta\nu \approx 1.0$ nm for $L = 1.35$ mm, which is close to the resolution of the spectrometer.

Figure 3b shows the SHG average output powers for three MIRO-101 crystals samples of similar millimeter size, but with different optical quality. The as-synthesized sample labeled "Raw A" developed a large screw dislocation during growth that covered a significant fraction of the optically-accessible crystal surface. Therefore, the output power was significantly lower (P_{SHG} < 10 µW) than the other samples. The second as-synthesized MIRO-101 crystal labelled in Figure 3b as "Raw B" was obtained after a careful control of the reaction and growth conditions was implemented.[35] The scattering losses were significantly reduced and nonlinear output powers up to ≈ 50 µW were achieved. After additional crystal engineering steps that included cutting and polishing, the high-quality optical crystals shown in Figure 1b were obtained. The input-output curve of the polished sample was used to estimate d_{eff} below. Figure 3c demonstrates that the measured scaling of the SHG signal with the pump power $P_{out} \approx P_{in}^\alpha$ is approximately quadratic ($\alpha \approx 2$) for all the crystal samples used, as expected from Equation 1.

As discussed above, a commercial BBO crystal with known d_{eff} was used as a reference to estimate d_{eff} for the polished MIRO-101 crystal sample, using the same optical setup. SHG measurements on the MOF sample were carried out at the phase matching angle $\theta_m = 25°$, which is close to the phase matching angle predicted for monochromatic pump (21, 7°, see Section S2, Supporting Information). At equal average pump power of $P_{MOF} = P_{BBO} = 10$ mW, for both crystals, the generated average output powers are $P_{SHG, MOF} = 0.30$ µW for MIRO-101 and $P_{SHG, BBO} = 550$ µW for BBO. Low pump powers are used to

**ADVANCED
SCIENCE NEWS**

www.advancedsciencenews.com

**ADVANCED
OPTICAL
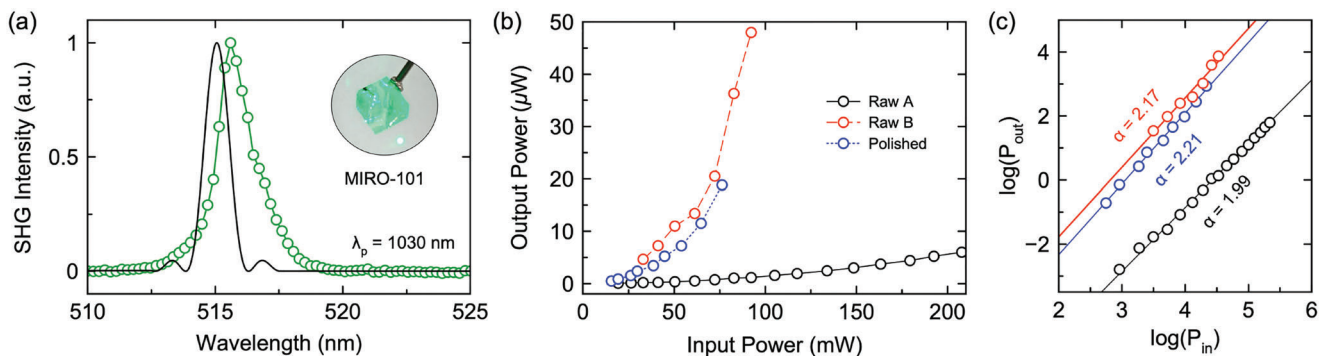MATERIALS**

www.advopticalmat.de

Figure 3. a) Measured SHG spectrum of a polished MIRO-101 MOF crystal illuminated by ultrafast 1030 nm pump pulses. The solid line shows the spectrum predicted from ab initio calculations. The inset shows SHG radiation produced by a raw sample.; b) SHG output power P_{out} for three MOF crystal samples with millimeter path lengths, as a function of the input pump power P_{in} at 1030 nm; c) Log–log plot of the nonlinear power scaling $P_{out} \approx P_{in}^\alpha$, showing quadratic behavior for all samples.

avoid pump depletion, self-focusing and thermal dephasing. The measured SHG power conversion ratio $P_{out}/P_{in} \approx 10^{-4}$ represents a lower bound of the up-conversion efficiency that should be expected for MIRO-101. The experimental setup can be further refined to maximize conversion efficiency by using longer pulses that match the spectral acceptance of the MOF crystal, Boyd-Kleinman focusing conditions, and suppressing Fresnel losses.

The effective nonlinearity $d_{eff,\,MOF}$ of MIRO-101 can be estimated using the value for BBO $d_{eff,\,BBO}$=1.94 pm V^{-1} for type-I ooe SHG at 1064 nm.[47] Using Equation 2 with the power output data in Figure 3b (polished sample), the uncorrected effective MOF nonlinearity is $d_{eff,\,MOF}$=0.038 pm V^{-1}. This estimate needs to be corrected by taking into account the spectral acceptance bandwidth of both crystals. The acceptance bandwidth for SHG at 515 nm is estimated to be $\Delta\lambda_{BBO}$=8.3 nm for BBO (L = 1.00 mm) and $\Delta\lambda_{MOF}$=1.1 nm for MIRO-101 (L = 1.35 mm). The spectral bandwidth of the pump pulses at 1030 nm is 12 nm, which is not much smaller than $2\Delta\lambda_{BBO}$ = 16.6 nm. This means that the BBO crystal phase–matches about 80% of the pump energy via birefringence phase matching , while the MOF crystal phase–matches much less. Taking into account the difference in spectral acceptance bandwidth, the bandwidth-corrected effective nonlinearity of MIRO-101 gives $d_{eff,MOF}$ = (80% × 8.3/1.1)$^{1/2}$ × 0.038 pm V^{-1} = 0.093 pm V^{-1}, where $P_{SHG} \propto d_{eff}^2$ was used.

Note that the pump laser, using CPA, does not generate Fourier-transform-limited pulses with a perfect temporal Gaussian profile, because then the bandwidth of the pulses would be 4.6 nm instead of 12 nm. It should also be noted that the effect of the external angular acceptance of both nonlinear crystals on SHG efficiency can be neglected because the L/b ratio is small, which was already pointed out. There is another difference between the two crystals, the BBO crystal has an antireflection coating and the MOF crystal does not. The reflectances of the BBO crystal are specified by the manufacturer as $R_{BBO,\,1030nm}$ = 0.033 and $R_{BBO,\,515nm}$ = 0.021. The reflectances of the MOF crystals can be obtained from the Sellmeier coefficients[40] and Fresnel's equations to give $R_{MOF,\,1030nm}$ = 0.083 (for n_o) and $R_{MOF,\,515nm}$ = 0.040 (for n_e). Using the transmittance, $T = 1 − R$, gives an improved

value of the effective nonlinear coefficient for MIRO-101 given by

$$d_{eff,MOF} = \frac{T_{BBO,1030nm}}{T_{MOF,1030nm}} \left(\frac{T_{BBO,515nm}}{T_{MOF,515nm}} \right)^{1/2} \times 0.093 \text{ pm V}^{-1}$$

$$= 0.10 \text{ pm V}^{-1} \tag{3}$$

This improved estimate is closer to the theoretical limit d_{eff} = 0.35 pm V^{-1},[40] and in principle can be further improved with additional crystal engineering steps. The nonlinearity of MIRO-101 MOF crystals under near-infrared pumping is comparable with typical nonlinear optical materials such as KDP (d_{36} = 0.38 pm V^{-1}, 1064 nm[47]) and α-SiO$_2$ (d_{11} = 0.30 pm V^{-1}, 1064 nm[48]).

2.4. Third-Harmonic Generation and Optical Damage

Figure 4a shows the coherent emission spectrum of a large polished MIRO-101 crystal (L = 1.35 mm) measured with an UV spectrometer, featuring an intense sharp peak centered at 342 nm, corresponding to the third-harmonic of the femtosecond pump laser pulses centered at λ_p = 1030 nm. THG produces an ultraviolet collimated beam that is visible on a fluorescent screen with the naked eye and propagates primarily in the forward direction with the well-defined angular distribution shown in Figure 4b. The THG signal was produced by rotating the crystal such that the polar angle with respect to the optic axis was θ = 34 ± 2 °. We infer that the THG signal corresponds to type-I ooe phase matching because the theoretical perfect phase matching angle is θ_m = 35.2°, from the Sellmeier equations for MIRO-101. For other phase-matching configurations, we expect θ_m = 42.3° for type-II ooee and θ_m = 58.5° for type-III oeee, which differ significantly from the observations. Further analysis of the polarization state of the THG output would be needed for a complete characterization of the wave mixing process.

The narrow angular distribution of THG in Figure 4b rules out three-photon pumped photoluminescence[49] and further supports the phase-coherent nature of the four-wave mixing process inside the MOF crystal. UV-specific optical elements would be
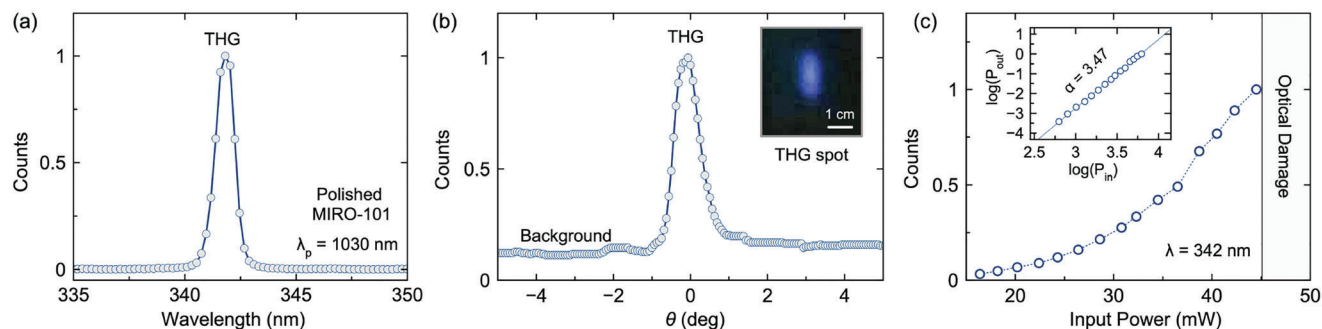
**ADVANCED
SCIENCE NEWS**

www.advancedsciencenews.com

**ADVANCED
OPTICAL
MATERIALS**

www.advopticalmat.de

Figure 4. a) Normalized THG spectrum of a polished MIRO-101 single crystal, illuminated by ultrafast 1030 nm pump laser pulses; b) Angular spread of the THG radiation produced by the MOF crystal. The inset shows an image of the blue THG spot produced on a screen 40 cm away from the MOF sample in the forward direction; c) Normalized THG intensity at 343 nm as a function of the input pump power. The log-log inset plot shows the approximate cubic scaling $P_{out} \approx P_{in}^{\alpha}$, and the shaded region marks intensities, where the THG signal is reduced by nonlinear absorption.
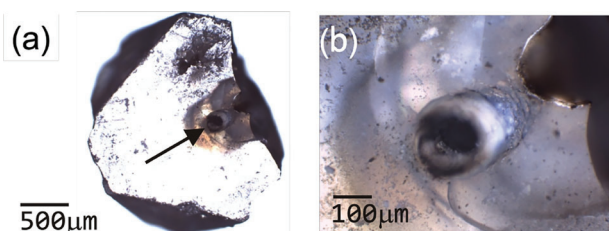

Figure 5. a) Laser-induced damage of a raw MIRO-101 MOF single crystal illuminated by intense 340 fs laser pulses at 1030 nm in air. The arrow indicates the hole produced via laser drilling. The right edge of the crystal was broken; b) Focused image of the hole surface.

needed to fully characterize the polarization state of the phase-matched THG signal. Figure 4c confirms the approximately cubic dependence of the THG signal with the average input power P_{in} of the pump pulses, as expected for a third-order nonlinear process.[14,15]

Pumping the MOF crystal sample with pulses stronger than about 45 mW average power produced a suppression of the nonlinear signal, keeping all other parameters constant. This could be due to persistent modifications of the local refractive index via self-focusing or local heat-induced chemical changes in the MOF structure. Both mechanisms would alter the four-wave mixing process and lead to a non-reversible decrease in the THG signal. For sufficiently intense pump pulses, the laser can drill holes into the MOF crystal that are a few times wider than the beam focus, as shown in **Figure 5**. The bulk damage threshold intensity of as-synthesized MOF crystals was estimated to be about 0.22 TW cm^{-2} with 340 fs pulses at 1030 nm (385 nJ pulse energy, 114 kHz repetition rate). Note that a fair comparison with other optical materials would require optical damage studies with nanosecond pulses.[50]

3. Conclusion

The linear and nonlinear optical properties of millimeter-sized noncentrosymmetric MOF crystals have been investigated using Zn(3-ptz)$_2$ (MIRO-101[35]) MOF single crystals with optimized morphology as a case study. MIRO-101 crystals are negative uniaxial with birefringence ($\Delta n = -0.34$) that supports phase-

matching conditions for feasible crystal rotation angles. The measured refractive indices n_o and n_e are in agreement with previous ab initio theoretical predictions for this MOF material.[40] The high transparency of MIRO-101 in the visible region is comparable to commercial nonlinear crystals such as BBO and KDP when Fresnel reflections are taken into account. The generation of second-harmonic (515 nm) and third-harmonic (343 nm) radiation from the same MOF single crystal was demonstrated for the first time. The frequency up-converted light is shown to preserve phase coherence when propagating inside the crystal over millimeter length scales, which is a significant improvement over previous reports of MOF nonlinear optical activity with powder samples,[51] as randomly oriented micron-size crystals cannot support long-range optical coherence. The effective nonlinear coefficient for SHG with collinear type-I (ooe) phase matching was measured to be $d_{eff} = 0.10$ pm V^{-1} at 1030 nm, which is close to the theoretical limit for this particular MOF material. Although the THG signal overlaps slightly with the band edge absorption of the sample, type-I oooe THG radiation is strongly emitted in the forward direction as a well-collimated beam.

When carrying out the up-conversion experiments, a temporal drift of the phase–matching angles could often be observed, which can be attributed to the thermal expansion of the MOF crystals. The MOF crystals only partially dissipate heat because the crystal holder is not made for this purpose. Crystal temperatures in the range 16–47 °C could be observed, depending on the average pump power. The phase–matching angles were determined experimentally at average pump powers corresponding to a crystal temperature of about 30 °C. The heat deposition in the crystal also has to be considered locally, because the Gaussian beam inside the crystal has a beam width $w_0 \approx 18\mu m$, i.e., a local transverse temperature gradient is created inside the crystal. This kind of local heating of a nonlinear crystal is known to cause thermal dephasing.[52] The temperature dependence of the refractive index creates different optical path lengths in the crystal, and the local mechanical stress generated by the local heat deposition produces stress–induced birefringence. This thermally induced phase mismatch inside the MOF crystal reduces the nonlinear efficiencies for SHG and THG. How intense the thermal dephasing is in the MOF crystals remains to be determined.

Our THG results with MIRO-101 single crystals expand the understanding of the third-order optical response of MOF

materials and complement recent Z-scan measurements of two-photon absorption and self-focusing of strong monochromatic laser beams using polycrystalline ZSTU-10[53] and NU-1000[54] MOFs at visible wavelengths (532 nm). Although these nonlinear absorption and dispersion measurements do not monitor the parametric processes involved in SHG and THG up-conversion processes, they reassure the high performance of MOF materials as nonlinear devices with increase photo-stability relative to conventional organic crystals.

Further crystal engineering efforts could further improve the intensity and spectral quality of up-converted light produced by pumping suitable MOF crystals with intense near-infrared pulses. The large second-order nonlinearities measured for millimeter-sized MIRO-101 crystals in this work, suggests that nonlinear optical devices based on MOFs may perform competitively relative to optical industry standards such as BBO and KDP, depending on the target application and operating conditions. Further experiments are needed to fully assess the real potential of MOF materials in nonlinear optics. This work thus paves the way for potential applications of MOF materials in bulk and integrated devices for applications in classical and quantum optical technology.

4. Experimental Section

MIRO-101 Single Crystals: The growth of millimeter-sized $Zn(3\text{-}ptz)_2$ MOF crystals by hydrothermal reaction of 3-cyanopyridine, sodium azide, and zinc acetate in the presence of nitric acid, was reported in Ref. [35]. The size and morphology of the single crystal product was controlled by optimizing the effective parameters that determine the growth and self-assembly of MOF crystals, such as the molar ratios of the reactants to ligand precursors, pH of the solution during mixing, level dilution of the mixture, total reaction volume, furnace absolute temperature and thermal fluctuations, and reaction time.[35,38] The reaction product consists of one or two large single crystals floating at the water/air interface, which favors the growth of deformed octahedral crystals with large parallel faces.[37] These crystals were suitable for the subsequent steps of cutting and polishing needed to enable phase matching in frequency up-conversion measurements. Optimum-size single crystals were achieved below pH 3.0 for 24 h at 105 °C, for a reactant molar ratio 2:4:6 (zinc acetate/3-cyanopyridine/sodium azide) in 7 mL total volume.

Supporting Information

Supporting Information is available from the Wiley Online Library or from the author.

Conflict of Interest

The authors declare no conflict of interest.

Data Availability Statement

The data that support the findings of this study are available from the corresponding author upon reasonable request.

[1] A. Radwan, H. Jin, D. He, S. Mu, *Nano-Micro Lett.* **2021**, *13*, 132.

[2] L. Chai, J. Pan, Y. Hu, J. Qian, M. Hong, *Small* **2021**, *17*, 2100607.

[3] K. Suresh, A. P. Kalenak, A. Sotuyo, A. J. Matzger, *Chem. A Eur. J.* **2022**, *28*, e202200334.

[4] S. Ma, H.-C. Zhou, *Chem. Commun.* **2010**, *46*, 44.

[5] D. Alezi, Y. Belmabkhout, M. Suyetin, P. M. Bhatt, Ł. J. Weseliński, V. Solovyeva, K. Adil, I. Spanopoulos, P. N. Trikalitis, A.-H. Emwas, M. Eddaoudi, *J. Am. Chem. Soc.* **2015**, *137*, 13308.

[6] Y. Liu, X.-Y. Xie, C. Cheng, Z.-S. Shao, H.-S. Wang, *J. Mater. Chem. C* **2019**, *7*, 10743.

[7] W. P. Lustig, S. Mukherjee, N. D. Rudd, A. V. Desai, J. Li, S. K. Ghosh, *Chem. Soc. Rev.* **2017**, *46*, 3242.

[8] X. F. Lu, Y. Fang, D. Luan, X. W. D. Lou, *Nano Lett.* **2021**, *21*, 1555.

[9] G. Xu, P. Nie, H. Dou, B. Ding, L. Li, X. Zhang, *Mater. Today* **2017**, *20*, 191.

[10] C. Wang, T. Zhang, W. Lin, *Chem. Rev.* **2012**, *112*, 1084.

[11] S. Du, H. Zhang, in *Metal-Organic Frameworks for Photonics Applications*, (Eds: B. Chen, G. Qian), Structure and Bonding, Springer, Berlin, Heidelberg **2014**, pp. 145–165.

[12] L. R. Mingabudinova, V. V. Vinogradov, V. A. Milichko, E. Hey-Hawkins, A. V. Vinogradov, *Chem. Soc. Rev.* **2016**, *45*, 5408.

[13] O. R. Evans, W. Lin, *Acc. Chem. Res.* **2002**, *35*, 511.

[14] R. W. Boyd, *Nonlinear Optics*, Academic Press, Cambridge, Massachusetts **2003**.

[15] M. Liu, H. S. Quah, S. Wen, Z. Yu, J. J. Vittal, W. Ji, *Chem. Mater.* **2016**, *28*, 3385.

[16] C. R. Groom, I. J. Bruno, M. P. Lightfoot, S. C. Ward, *Acta Crystallographica Section B: Structural Science, Crystal Engineering and Materials* **2016**, *72*, 171.

[17] Y. R. Shen, *Annu. Rev. Mater. Sci.* **1986**, *16*, 69.

[18] C. Gmachl, A. Belyanin, D. Sivco, M. Peabody, N. Owschimikow, A. Sergent, F. Capasso, A. Cho, *IEEE J. Quantum Electron.* **2003**, *39*, 1345.

[19] P. Campagnola, *Anal. Chem.* **2011**, *83*, 3224.

[20] I. Aramburu, J. Ortega, C. L. Folcia, J. Etxebarria, *Appl. Phys. B: Lasers Opt.* **2014**, *116*, 211.

[21] S. K. Kurtz, T. T. Perry, *J. Appl. Phys.* **1968**, *39*, 3798.

[22] K. M. Ok, E. O. Chi, P. S. Halasyamani, *Chem. Soc. Rev.* **2006**, *35*, 710.

[23] V. G. Dmitriev, G. G. Gurzadyan, D. N. Nikogosyan, *Handbook of Nonlinear Optical Crystals*, vol. *64* of *Springer Series in Optical Sciences*, Springer Berlin Heidelberg, Berlin, Heidelberg **1991**.

[24] D. F. Eaton, *Science* **1991**, *253*, 281.

[25] N. Gisin, R. Thew, *Nat. Photonics* **2007**, *1*, 165.

[26] J. L. O'Brien, A. Furusawa, J. Vučković, *Nat. Photonics* **2009**, *3*, 687.

[27] B. Liu, K. Vellingiri, S.-H. Jo, P. Kumar, Y. S. Ok, K.-H. Kim, *Nano Res.* **2018**, *11*, 4441.

[28] A. G. Zavyalova, D. V. Kladko, I. Y. Chernyshov, V. V. Vinogradov, *J. Mater. Chem. A* **2021**, *9*, 25258.

[29] G. Rodrigo, R. Ballesteros-Garrido, *Dalton Trans.* **2022**, *51*, 7775.

[30] I. Chi-Durán, J. Enríquez, C. Manquian, K. Wrighton-Araneda, W. Cañon-Mancisidor, D. Venegas-Yazigi, F. Herrera, D. P. Singh, *ACS Omega* **2018**, *3*, 801.

**ADVANCED
SCIENCE NEWS**

www.advancedsciencenews.com

**ADVANCED
OPTICAL
MATERIALS**

www.advopticalmat.de

[31] M. Xu, B. Liu, L. Zhang, H. Ren, Q. Gu, X. Sun, S. Wang, X. Xu, *Light: Sci. Appl.* **2022**, *11*, 241.

[32] M. J. Van Vleet, T. Weng, X. Li, J. Schmidt, *Chem. Rev.* **2018**, *118*, 3681.

[33] Y. J. Colón, A. Z. Guo, L. W. Antony, K. Q. Hoffmann, J. J. de Pablo, *The Journal of Chemical Physics* **2019**, *150*, 104502,

[34] A. Sorrenti, L. Jones, S. Sevim, X. Cao, A. J. deMello, C. Martí-Gastaldo, J. Puigmartí-Luis, *J. Am. Chem. Soc.* **2020**, *142*, 9372.

[35] J. M. Garcia-Garfido, J. Enríquez, I. Chi-Durán, I. Jara, L. Vivas, F. J. Hernández, F. Herrera, D. P. Singh, *ACS Omega* **2021**, *6*, 17289.

[36] L.-Z. Wang, Z.-R. Qu, H. Zhao, X.-S. Wang, R.-G. Xiong, Z.-L. Xue, *Inorg. Chem.* **2003**, *42*, 3969.

[37] I. Chi-Durán, R. A. Fritz, R. Urzúa-Leiva, G. Cárdenas-Jirón, D. P. Singh, F. Herrera, *ACS Omega* **2022**, *7*, 24432.

[38] J. Enríquez, C. Manquian, I. Chi-Duran, F. Herrera, D. P. Singh, *ACS Omega* **2019**, *4*, 7411.

[39] V. Kolchinskiy, C. H. Shih, I. Lo, R. Romashko, *Physics Procedia* **2017**, *86*, 176.

[40] R. A. Fritz, Y. J. Colón, F. Herrera, *Chem. Sci.* **2021**, *12*, 3475.

[41] S. D. H. Andéasson, S. E. Gttstaesson, N.-O. Halling, *JOSA* **1971**, *61*, 595.

[42] M. Elshazly-Zaghloul, R. M. A. Azzam, *JOSA* **1982**, *72*, 657.

[43] J. Lekner, *J. Phys.: Condens. Matter* **1991**, *3*, 6121.

[44] G. D. Boyd, D. A. Kleinman, *J. Appl. Phys.* **1968**, *39*, 3597.

[45] D. L. S. F. M. Dickey, S. C. Holswade, *Laser Beam Shaping Applications*, Taylor & Francis Group, London **2006**.

[46] R. L. Sutherland, D. G. McLean, S. Kirkpatrick, *Handbook of nonlinear optics*, Number 82 in Optical engineering. 2nd Ed., rev. and expanded edition, Marcel Dekker, New York **2003**.

[47] R. C. Eckardt, R. L. Byer, in *Inorganic Crystals for Optics, Electro-Optics, and Frequency Conversion*, vol. *1561*, SPIE Bellingham, WA **1991**.

[48] K. Hagimoto, A. Mito, *Appl. Opt.* **1995**, *34*, 8276.

[49] H. He, E. Ma, Y. Cui, J. Yu, Y. Yang, T. Song, C.-D. Wu, X. Chen, B. Chen, G. Qian, *Nat. Commun.* **2016**, *7*, 11087.

[50] O. Uteza, B. Bussière, F. Canova, J. P. Chambaret, P. Delaporte, T. Itina, M. Sentis, *Appl. Surf. Sci.* **2007**, *254*, 799.

[51] R. Medishetty, J. K. Zareba, D. Mayer, M. Samoc, R. A. Fischer, *Chem. Soc. Rev.* **2017**, *46*, 4976.

[52] Y. K. Yap, K. Deki, N. Kitatochi, Y. Mori, T. Sasaki, *Opt. Lett.* **1998**, *23*, 1016.

[53] R. Abazari, E. Yazdani, M. Nadafan, A. M. Kirillov, J. Gao, A. M. Z. Slawin, C. L. Carpenter-Warren, *Inorg. Chem.* **2021**, *60*, 9700.

[54] Y. Pan, S. Sanati, M. Nadafan, R. Abazari, J. Gao, A. M. Kirillov, *Inorg. Chem.* **2022**, *61*, 18873.

2300142 (8 of 8)